



OPEN

Design, preparation and application of the semicarbazide-pyridoyl-sulfonic acid-based nanocatalyst for the synthesis of pyranopyrazoles

Masoumeh Beiranvand & Davood Habibi✉

A novel, efficient, and recoverable nanomagnetic catalyst bearing the semicarbazide linkers, namely, $\text{Fe}_3\text{O}_4@\text{SiO}_2@\text{OSi}(\text{CH}_2)_3\text{-N}(3\text{-pyridoyl sulfonic acid})\text{semicarbazide}$ (FSiPSS) was designed, synthesized and characterized by the use of various techniques such as FT-IR, EDX, elemental mapping analysis, XRD, SEM, TEM, TGA/DTA, BET, and VSM. Then, the catalytic capability of the novel prepared nanomagnetic FSiPSS catalyst was successfully investigated in the synthesis of diverse pyranopyrazoles through a one-pot four-component condensation reaction of ethyl acetoacetate, hydrazine hydrate, aromatic aldehydes, and malononitrile or ethyl cyano-acetate by the help of ultrasonication in very short reaction time, good to high yields and easy work-up (Fig. 1).

Semicarbazide (SEM) is a derivative of urea or hydrazine that possess several important functions in medicinal and health-related issues. SEM motifs constitute the core structures of several drugs and herbicides such as nitrofurazone, tolazamide, larmustine, cafenstrole, and diflufenzopyr^{1–3}. In addition, SEM is applied in food as a marker to detect the illegal usage of the banned antibiotic nitrofurazone⁴. They also reveal a stabilizing effect on the liquid crystalline state of chloroplast membrane lipids, and some are known as surfactants. Another report exhibited that SEMs are also applied as stabilizing agents in the polymer industry⁵.

Also, magnetic nanoparticles (MNPs) are receiving increasing interest due to their widespread applications in various fields. MNPs have many advantages in organic chemistry, (1) MNPs are accessible; (2) the stability of catalyst linkages leads to the use of more environmentally friendly solvents than homogeneous catalysis; (3) simple separation by an external magnetic field; (4) the fabrication of MNPs is generally simple, scalable, safe, cost-effective and controllable; (5) catalyst leaching is usually lower than other material-supported catalysts⁶. Many reports on MNPs nanoparticles have appeared over during years^{7–11}. Among different types of MNPs, aluminum and iron oxide have large advantages such as low cost, extensive availability, thermal stability, and considerable adsorption capacity¹².

In particular, iron oxide nanoparticles (IONPs), which belong to the ferrimagnetic class of magnetic materials, are widely applied in the fields of biomedicine and bioengineering due to their ease of surface modification, synthesis, and low toxicity. Magnetite (Fe_3O_4) and maghemite ($\gamma\text{-Fe}_2\text{O}_3$) and mixed ferrites (MFe_2O_4 where $\text{M}=\text{Co}, \text{Mn}, \text{Ni}, \text{or Zn}$) are the three main forms of iron oxide-based nanoparticles^{13–16}. To prevent the aggregation of MNPs and also enhancement their stability of them, usually, a layer of silica is coated on the surface¹⁷. Fe_3O_4 coated with silica was often used as the support of metal and nonmetal catalysts^{18–21}.

Magnetic nanomaterials are more efficient adsorbents than active carbon, graphene oxide (GO), and zeolite-based adsorbents due to their ease of removal of contaminants from wastewater employing an applied magnetic field but also their advantageous surface charge and redox activity characteristics. The incorporation of magnetic nanomaterials with adsorbents such as WO_3 , TiO_2 , ZnO , and GO decreases the rapid recombination of photoinduced electron holes and improves the photocatalysis potential of these materials. On the other hand, magnetic nanomaterials can a synergistic effect with biosorbents. Biosorbents possess efficient adsorption capacity to eliminate pollutants, and high abundance and therefore help diminish ecological and environmental problems^{22,23}.

Department of Organic Chemistry, Faculty of Chemistry, Bu-Ali Sina University, Hamedan, Iran. ✉email: davood.habibi@gmail.com

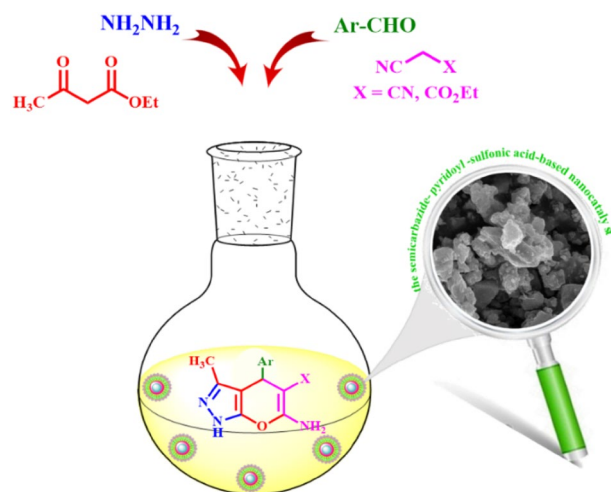


Figure 1. Synthesis of diverse pyranopyrazoles by the FSiPSS nano-catalyst.

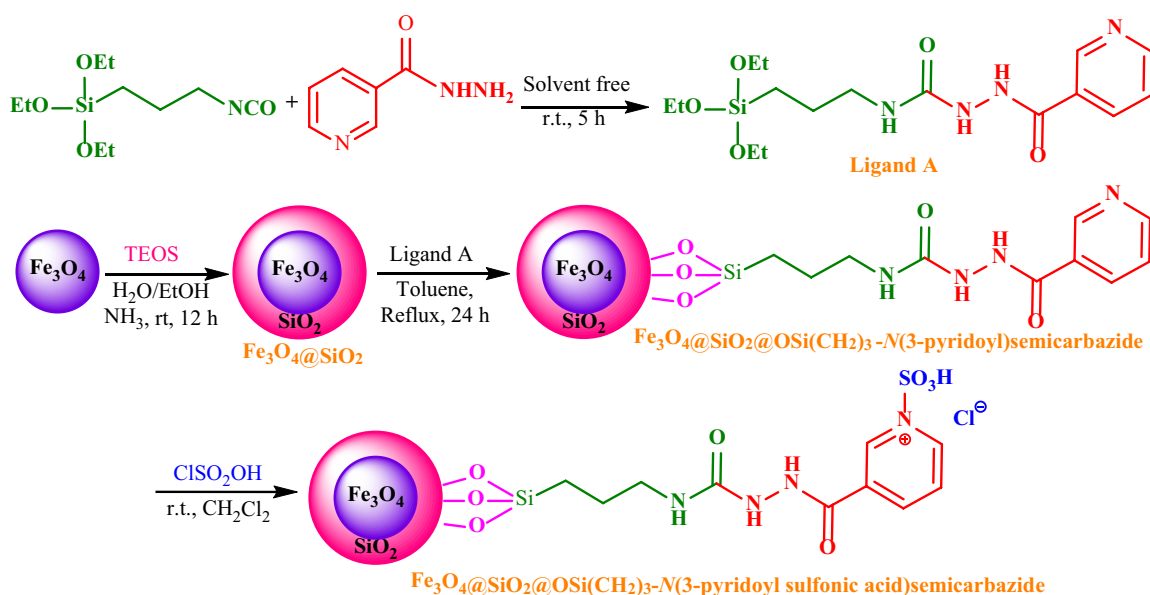


Figure 2. Synthesis of the FSiPSS nano-catalyst.

Among iron oxide magnetic nano-particles, sulfonic acid-functionalized magnetic nanoparticles, known as the recoverable solid strong acid, have attracted much attention due to economically important and environmentally benign features²⁴.

In addition, pyranopyrazoles (six-membered oxygen-containing heterocycles) have received considerable attention due to the wide range of biological activities such as anti-cancer, anti-leishmanial, antimicrobial, anti-inflammatory, lactamase inhibitor, etc.^{25–28}. Three-component (3-CR) or four-component (4-CR) reactions are often used for the synthesis of pyranopyrazoles²⁹. Several methods have been established for their synthesis using copper-immobilized ionic liquid³⁰, *N*-methylmorpholine *N*-oxide and silver oxide (Ag₂O)³¹, isonicotinic acid³², cetyltrimethylammonium chloride (CTACl)³³, [bmim]BF₄³⁴, choline chloride-urea deep eutectic solvent³⁵, bael fruit ash (BFA)-catalyst³⁶, P₂O₅/SiO₂ or H₃PO₄/Al₂O₃³⁷, Nd-salen Schiff base complex immobilized mesoporous silica³⁸, uncapped SnO₂ quantum dots (QDs)³⁹, sodium citrate⁴⁰, trityl carbocation⁴¹, CeO₂/ZrO₂⁴², saccharose⁴³, per-6-amino-β-cyclo-dextrin (per-6-ABCD)⁴⁴, 2-carboxy-*N,N*-diethylethan-aminium acetate⁴⁵, cinchona alkaloid⁴⁶, 4CzIPN/Ni⁰-metallaphotoredox⁴⁷, sodium ascorbate⁴⁸ and Meglumine⁴⁹.

In this paper and following our interests to present new and efficient protocols for the synthesis of biologically valuable structures by the use of nanomagnetic catalysts^{50–54}, we would like to report the rational design, synthesis, and characterization of the novel FSiPSS nano-catalyst (Fig. 2).

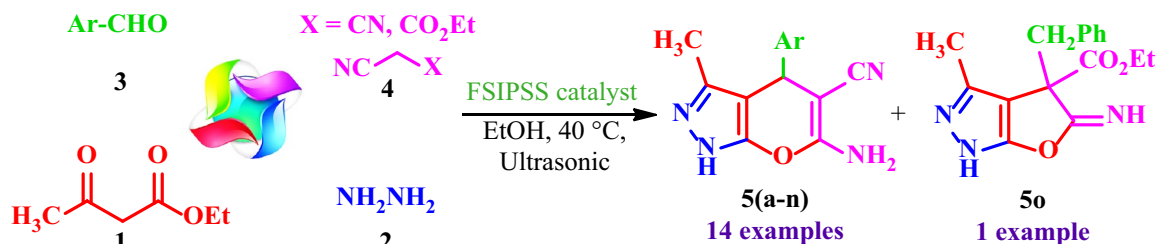


Figure 3. Synthesis of pyranopyrazoles.

Then, the FSiPSS nano-catalyst was used as an efficient heterogeneous catalyst for the synthesis of pyranopyrazoles via a one-pot four-component condensation reaction of ethyl acetoacetate **1**, hydrazine hydrate **2**, aromatic aldehydes **3**, and malononitrile or ethyl-cyano-acetate **4** under ultrasonic conditions (Fig. 3).

Experimental

General. All the commercial reagents were obtained from the Merck or Aldrich chemical companies and used without further purification. The reaction progress and purity of the synthesized compounds were monitored by TLC performed with silica gel 60 F-254 plates. FT-IR spectra were recorded on a PerkinElmer Spectrum Version 10.02.00 using KBr pellets. The ^1H NMR (250 MHz) and ^{13}C NMR (62.5 MHz) spectra were recorded on a Bruker spectrometer (δ in ppm) using DMSO- d_6 as a solvent with chemical shifts measured relative to TMS as the internal standard. Melting points were taken with a BUCHI 510 melting point apparatus. Elemental analysis was done using a MIRA II analyzer. The TEM images were recorded on a CM120 total carbon analyzer. The FESEM images were recorded using a MIRA III analyzer. The X-ray diffraction (XRD) measurements were performed with an XRD Philips PW1730. Thermogravimetric-differential thermal analysis (TG-DTA) was carried out using an SDT-Q600 device. A 2200 ETH-SONICA ultrasound cleaner (50 Hz) was employed for ultrasonication purposes.

A novel, efficient, and recoverable nanomagnetic catalyst bearing semicarbazide linker, namely, $\text{Fe}_3\text{O}_4@\text{SiO}_2@\text{OSi}(\text{CH}_2)_3\text{-N}(3\text{-pyridoyl sulfonic acid})\text{semicarbazide}$ was designed, synthesized, and characterized using various techniques including Fourier transform infrared (FT-IR) spectroscopy, energy dispersive X-ray (EDX) analysis, elemental mapping analysis, X-ray diffraction (XRD), scanning electron microscopy (SEM), transmission electron microscopy (TEM), thermo-gravimetric analysis/differential thermal analysis (TGA/DTA), vibrating sample magnetometer (VSM) and Brunauer–Emmett–Teller (BET).

General procedure for preparation of the ligand A. Initially, ligand A (2-nicotinoyl-*N*-(3-(triethoxysilyl)propyl)hydrazine-1-carboxamide) was prepared through the reaction of triethoxy(3-isocyanatopropyl)silane (1.237 g, 5 mmol) and nicotinic acid hydrazide (685 mg, 5 mmol) under solvent-free conditions at room temperature for 5 h. Then, the resulting pale-yellow precipitate was washed with a mixture of *n*-hexane and dichloromethane (3×10 mL). The obtained product was air-dried and characterized using FT-IR, ^1H NMR, and ^{13}C NMR.

General procedure for the construction of $\text{Fe}_3\text{O}_4@\text{SiO}_2@\text{OSi}(\text{CH}_2)_3\text{-N}(3\text{-pyridoyl sulfonic acid})\text{semicarbazide}$ (FSiPSS). The FSiPSS nano-catalyst was prepared in the following four consecutive stages:

Stage 1: The Fe_3O_4 magnetic nanoparticles (MNPs) were prepared based on the literature⁵⁵. The mixture of $\text{FeCl}_3 \cdot 6\text{H}_2\text{O}$ (11.44 g, 42.39 mmol) and $\text{FeCl}_2 \cdot 4\text{H}_2\text{O}$ (4.3 g, 21.62 mmol) was dissolved in water (100 mL) and stirred for 30 min at 80 °C. Then, the 37% ammonia solution (20 mL) was added dropwise to the resulting mixture and heated at 70 °C with vigorous stirring in pH 10 for 0.5 h. After separation by an external super magnet, a black precipitate ($\text{Fe}_3\text{O}_4 = \text{F}$) was filtered, washed with water, and air-dried.

Stage 2: The surface of the obtained Fe_3O_4 MNPs was coated with SiO_2 layers⁵⁶. Fe_3O_4 -MNPs (2.0 g) were dispersed in a mixture of EtOH and deionized water (250 ml, V/V = 4:1) under ultrasonic conditions for 15 min. Then, $\text{NH}_3 \cdot \text{H}_2\text{O}$ (3 mL) and TEOS (2 mL) were slowly added dropwise and the mixture was stirred for a further 12 h. $\text{Fe}_3\text{O}_4@\text{SiO}_2$ (FSi) were collected by magnetic separation, washed with water and ethanol, and vacuum dried.

Stage 3: The surface of $\text{Fe}_3\text{O}_4@\text{SiO}_2$ was functionalized with the ligand A. So, $\text{Fe}_3\text{O}_4@\text{SiO}_2$ (1.0 g) was mixed with ligand A (0.768 g, 2 mmol) under refluxing anhydrous toluene for 48 h. Then, the obtained $\text{Fe}_3\text{O}_4@\text{SiO}_2@\text{OSi}(\text{CH}_2)_3\text{-N}(3\text{-pyridoyl})\text{semicarbazide}$ (FSiPS) was separated with a super magnet, washed with ethanol, and vacuum dried.

Stage 4: Further functionalization of $\text{Fe}_3\text{O}_4@\text{SiO}_2@\text{OSi}(\text{CH}_2)_3\text{-N}(3\text{-pyridoyl})\text{semi-carbazide}$ was done with chlorosulfuric (chlorosulfonic) acid (0.133 mL, 233 mg, 2 mmol) in CH_2Cl_2 at ice bath. Then, the precipitate (FSiPSS) was separated with a super magnet, washed with CH_2Cl_2 and air-dried. The structure and morphology of FSiPSS were fully confirmed by various techniques.

General procedure for the synthesis of pyranopyrazoles catalyzed by FSiPSS. A mixture of ethyl acetoacetate **1** (0.130 g, 1.0 mmol), hydrazine hydrate **2** (0.032 g, 1.0 mmol), aromatic aldehydes **3** (1.0 mmol), malononitrile **4a** or ethyl cyanoacetate **4b** (1.5 mmol) and FSiPSS (20 mg) was heated at 40 °C under ultrasonic irradiation in EtOH (5 mL). Reaction progress was monitored by TLC (*n*-hexane/EtOAc). After completion of

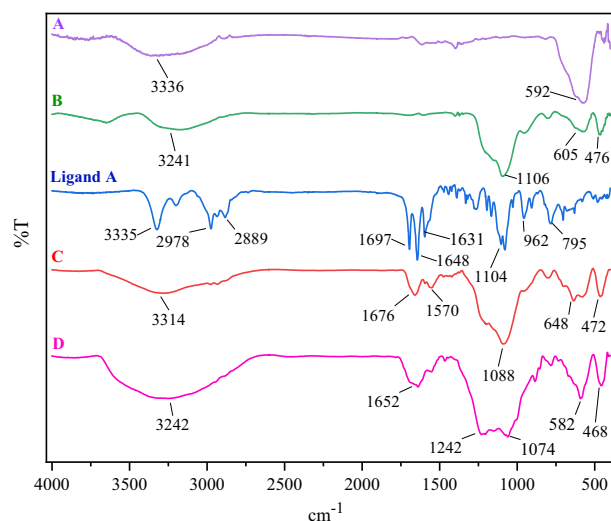


Figure 4. FT-IR spectra of FSiPSS and the corresponding compounds.

the reaction, the FSiPSS nano-catalyst was separated by a super magnet, the pure products obtained by recrystallization in ethanol and characterized by FT-IR, NMR, and mass spectrometry techniques.

Results and discussion

The formation of the FSiPSS nano-catalyst was confirmed by various techniques involving FT-IR, EDX, VSM, XRD, SEM, TEM, TGA/DTA, and BET.

Characterization of the FSiPSS nanocatalyst by FT-IR. In a comparative exploration as indicated in Fig. 4, the FT-IR spectra of **A**: Fe_3O_4 , **B**: $\text{Fe}_3\text{O}_4@\text{SiO}_2$, the ligand **A**, **C**: $\text{Fe}_3\text{O}_4@\text{SiO}_2@\text{OSi}(\text{CH}_2)_3\text{-N}(3\text{-pyridoyl})\text{semicarbazide}$ and **D**: $\text{Fe}_3\text{O}_4@\text{SiO}_2@\text{OSi}(\text{CH}_2)_3\text{-N}(3\text{-pyridoyl sulfonic acid})\text{semicarbazide}$ were explored. The peak at about 592 cm^{-1} is related to the presence of the Fe–O stretching vibrations in the curve of Fe_3O_4 . The FT-IR spectrum of $\text{Fe}_3\text{O}_4@\text{SiO}_2$ involves a new peak at 1106 cm^{-1} which is related to the Si–O–Si absorption band. FT-IR spectrum of synthesized ligand A shows three basic characteristic peaks at 3335, 1697, and 1648 cm^{-1} indicating the presence of the NH, C=O, and C=N bonds respectively. The spectrum of $\text{Fe}_3\text{O}_4@\text{SiO}_2@\text{OSi}(\text{CH}_2)_3\text{-N}(3\text{-pyridoyl})\text{semicarbazide}$ exhibits all above mentioned characteristic peaks. Finally, the broad peak from $2700\text{ to }3700\text{ cm}^{-1}$ shows the existence of acidic OH and NH functional groups within the structure of the desired catalyst. Consequently, the comparison of all the IR spectra confirms the successful construction of the semicarbazide-pyridoyl-sulfonic acid-based nano-catalyst.

Characterization of the FSiPSS nanocatalyst by EDX and elemental mapping analysis. As shown in Figs. 5 and 6, the obtained results from both EDX and elemental mapping analysis confirmed the existence of Fe, Si, O, C, N, S, and Cl elements in the structure of the synthesized nanocatalyst. The percentages of each element are presented in Table 1.

Characterization of the FSiPSS nanocatalyst by VSM. In another study, VSM analysis was performed for the exploration of the magnetic behavior of the FSiPSS nano-catalyst (**D**) and the corresponding compounds (**A**, **B**, **C**). As illustrated in Fig. 7, decrease saturation magnetization from about 70 emu g^{-1} (for major core Fe_3O_4) to about 10 emu g^{-1} for the FSiPSS nano-catalyst is related to the newly coated layer which can be explained by the reduction in the dipole–dipole interactions between the magnetic nanoparticles after their coating with SiO_2 and functionalization with ligand A and chlorosulfonic acid.

Characterization of the FSiPSS nano-catalyst by the SEM. To study the particle size and surface morphology of the newly prepared catalyst, SEM images were also taken. The resulting images are exposed in Fig. 8. According to these images, the sizes of the FSiPSS nano-catalyst particles are in the nanometer ranges (between 13.66 and 35.86 nm).

Characterization of the FSiPSS nano-catalyst by the TEM images. The obtained TEM images also proved that the sizes of the FSiPSS nano-catalyst particles are in the nanometer ranges, as shown in Fig. 9. Moreover, the core–shell structure of the nano-catalyst can be apperceived through TEM images.

At a closer investigation, as illustrated in the particle size distribution histograms (Fig. 10), the sizes of the nanoparticles are between 5 and 20 nm, and the average particle size is evaluated at about 9.61 nm.

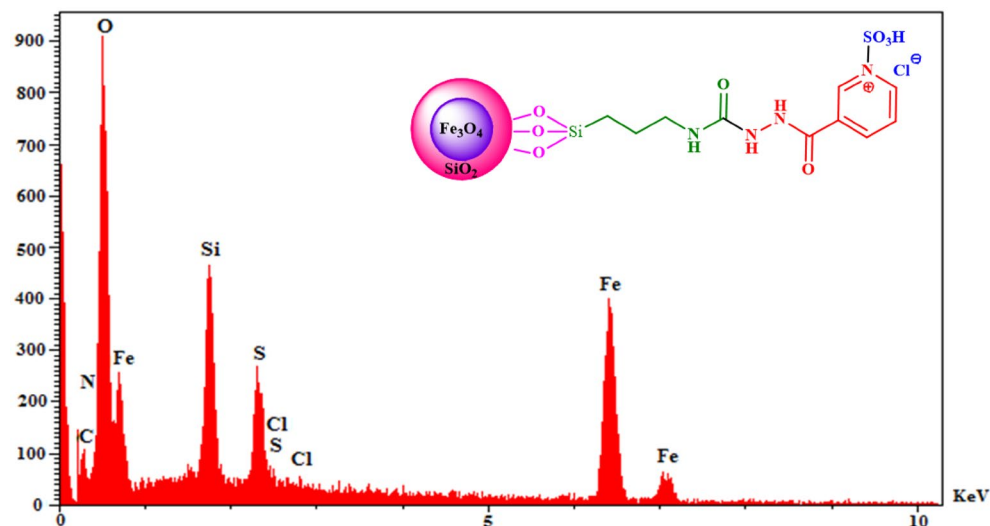


Figure 5. The EDX analysis of the FSiPSS nano-catalyst.

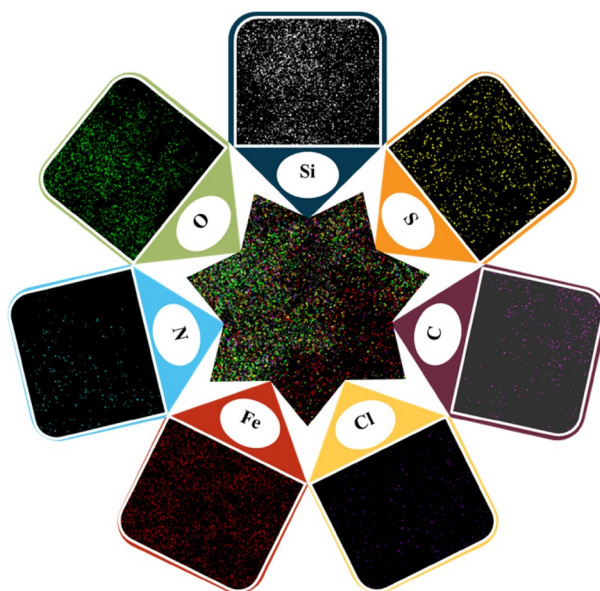


Figure 6. Elemental mapping analysis of the FSiPSS nano-catalyst.

Element	Fe	Si	O	C	N	S	Cl
W%	29.98	5.72	39.99	11.69	9.87	3.44	0.31

Table 1. The percentages of each element in EDX analysis.

Characterization of the FSiPSS nano-catalyst by TGA-DTA. In addition, TGA-DTA analysis was applied to investigate the thermal behavior of the FSiPSS nano-catalyst. The obtained curve is presented in Fig. 11. The thermo-gravimetric curve displays the three mass losses upon heating. The weight loss from about 60–120 °C (23%) can be attributed to the loss of water molecules, the weight loss from 120 to 300 °C (7%) can be related to the decomposition of acidic functional groups and the weight loss from 300 to 650 °C (17%) can be attributed to the decomposition of the ligand A. Also, about 72% of the initial mass remains at 700 °C.

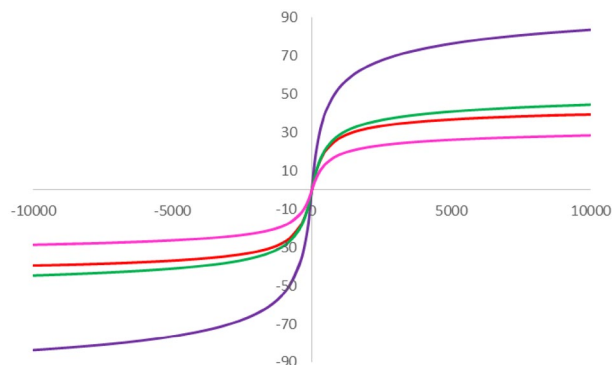


Figure 7. The VSM analyses of A, B, C and D.

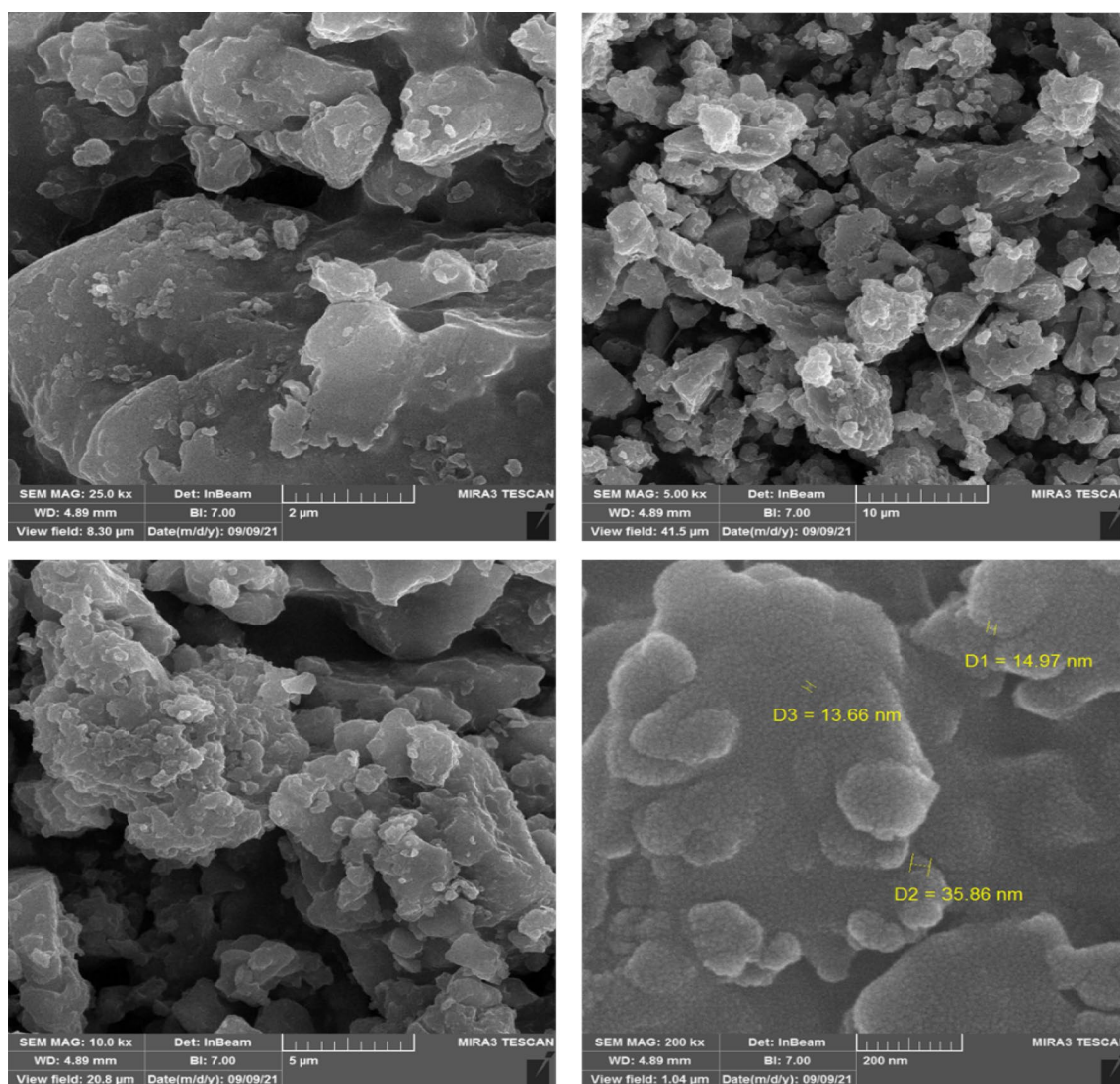


Figure 8. The SEM images of the FSiPSS nano-catalyst.

Characterization of the FSiPSS nano-catalyst by XRD. Crystalline phases and the diffraction planes of FSiPSS nanocomposites were ascertained by the XRD study, as presented in Fig. 12. FSiPSS pattern represents a single-phase profile indicating a united entity of the assembled counterparts. The typical diffraction peaks, due to the FSiPSS nano-catalyst are observed at $2\theta = 30.1, 35.5, 43.1, 53.5, 57,$ and 62.8 , corresponding to (220), (311), (400), (422), (511) and (440) Miller indices, respectively (ICDD, PDF, file no. 01-075-0033)⁵⁶. The

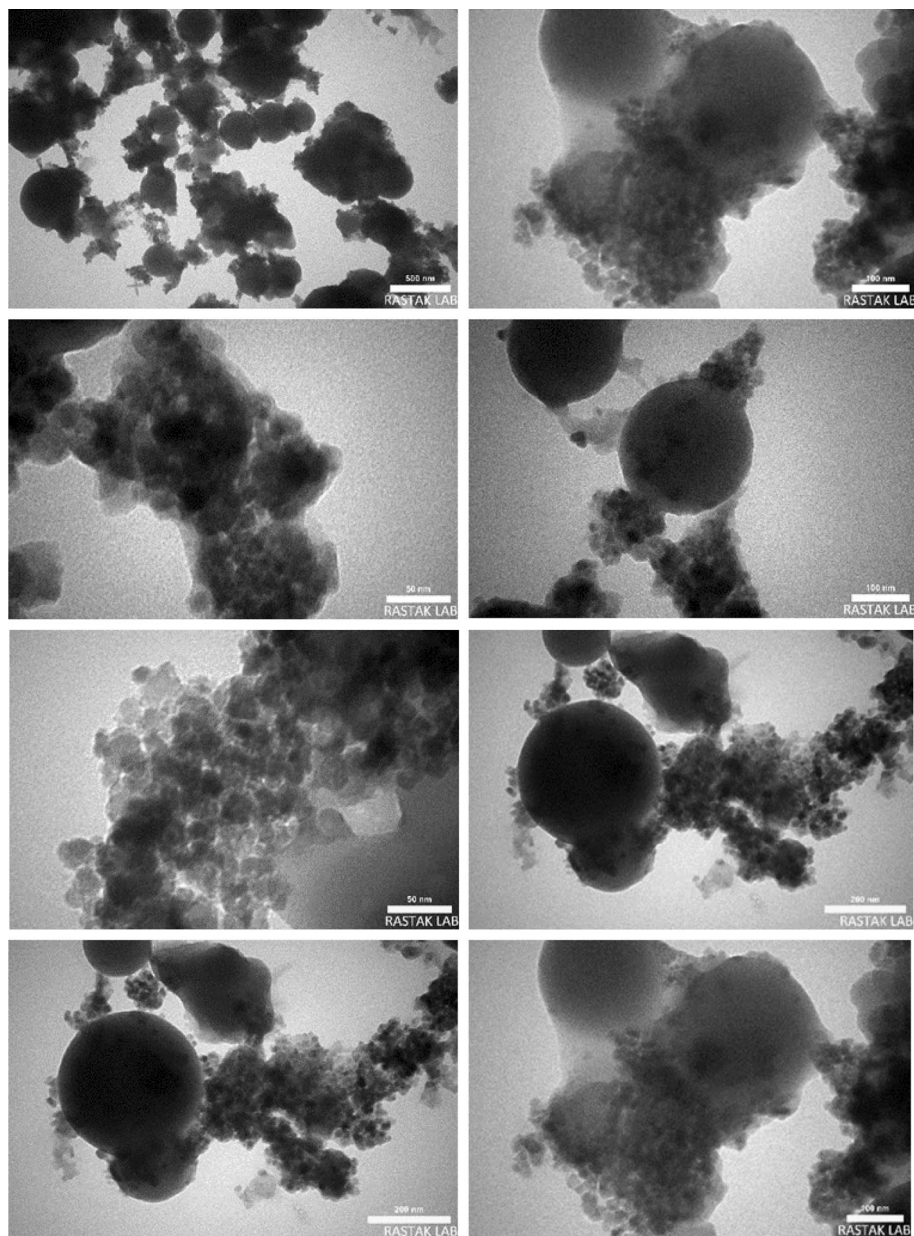


Figure 9. The TEM images of the FSiPSS nano-catalyst.

obtained pattern is in good agreement with the characteristic peaks of bare Fe_3O_4 which indicates the retention of the crystalline spinel ferrite core structure during the functionalization of MNPs and the successful synthesis of desired catalyst⁵⁷. In addition, the successful synthesis of $\text{Fe}_3\text{O}_4@SiO_2$ core-shell was confirmed by the presence of a broad peak at $2\theta = 20^\circ - 30^\circ$ which is due to the amorphous silicon layer, demonstrating that the magnetic moiety structure was protected in the core where SiO_2 cover did not alter the crystal structure of the magnetic Fe_3O_4 nanoparticles⁵⁸. In addition, after anchoring the $OSi(CH_2)_3-N(3\text{-pyridoyl sulfonic acid})$ semicarbazide functional groups, the peaks were found to have background noise levels increased, that coming from the amorphous added sulfonic acid functionalities⁵⁹. Finally, based on the Scherrer equation ($D = K\lambda/(\beta \cos \theta)$), the average crystallite size of FSiPSS nanocomposites was found to be about 16.27 nm.

Characterization of the FSiPSS nano-catalyst by BET. The specific surface area of the synthesized catalyst was determined by the N_2 adsorption-desorption analysis. The specific surface area, the total pore volumes (V_{total}), the pore diameters (DBJH), and the wall thickness of the samples were inspected at 77 Kelvin for 6 h. The results indicate that according to the IUPAC classification of adsorption isotherms⁶⁰, the N_2 isotherm resembles the type III (Fig. 13). The obtained results of BET measurements were represented in Table 2. According to the obtained data, the surface area of the catalyst is $35.6 \text{ m}^2 \text{ g}^{-1}$, which can provide a sufficient surface area for the catalyst to perform the desired synthesis.

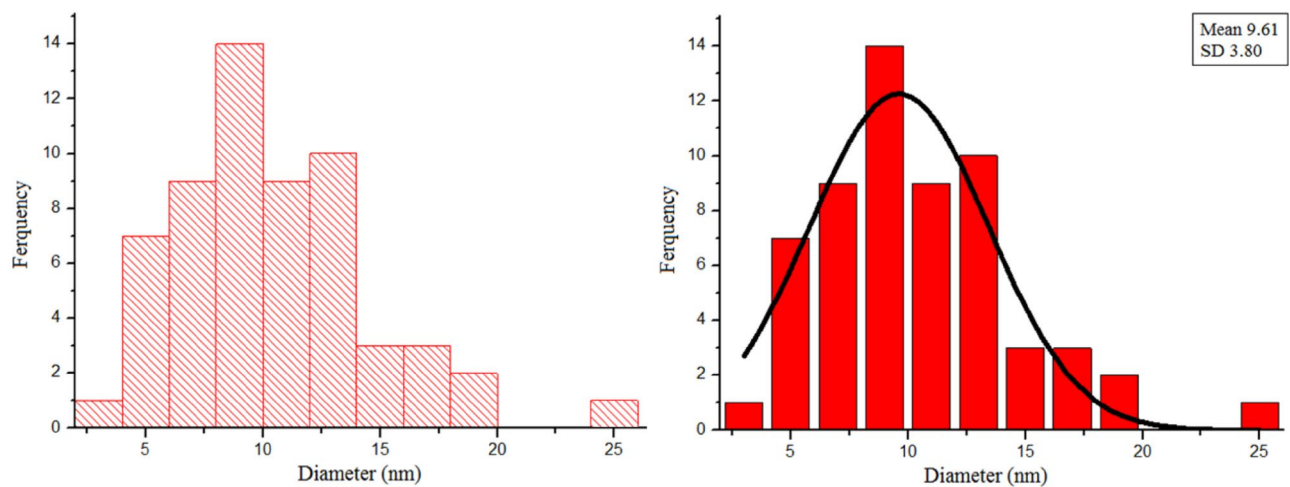


Figure 10. The particle size distribution (histogram) of the FSiPSS nano-catalyst.

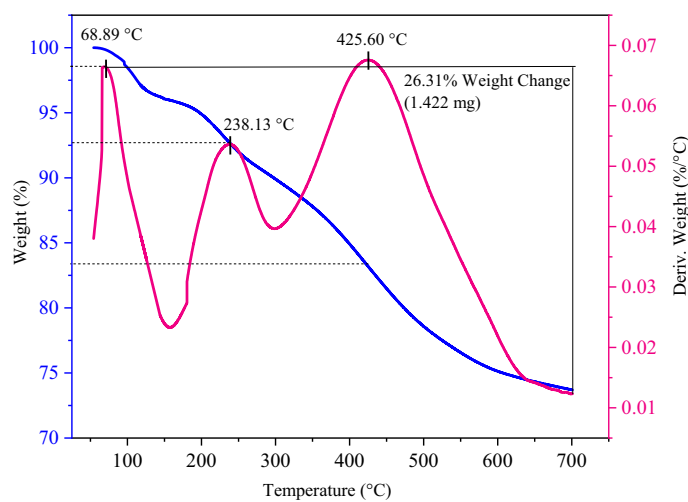


Figure 11. The TGA-DTA patterns of the FSiPSS nano-catalyst.

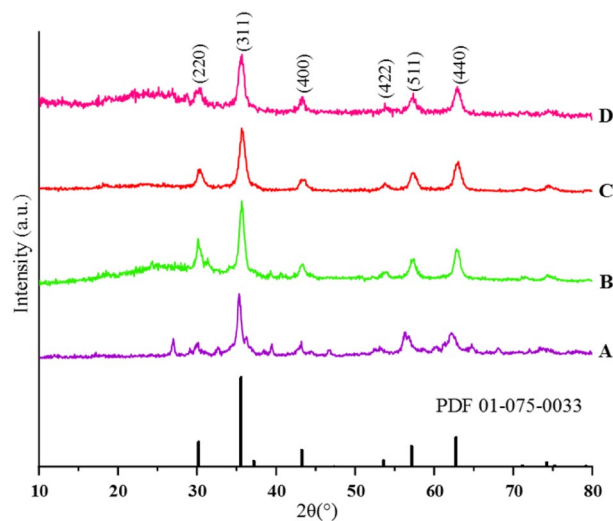


Figure 12. The XRD patterns of A, B, C, D and simulated pattern of the structure.

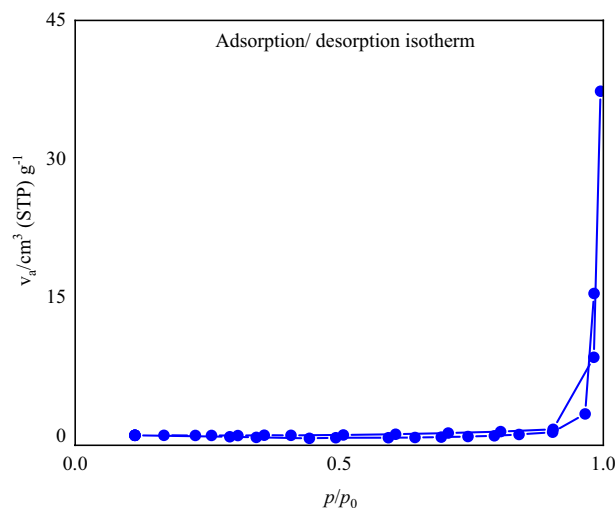


Figure 13. The nitrogen adsorption–desorption curve (BET) of the FSiPSS nano-catalyst.

Parameter	Value
a_s ($\text{m}^2 \text{g}^{-1}$)	3.56
V_m ($\text{cm}^3 \text{g}^{-1}$)	8.17
Total pore volume	4.11
Mean pore diameter	462.19

Table 2. Results from the BET measurements of the FSiPSS nano-catalyst.

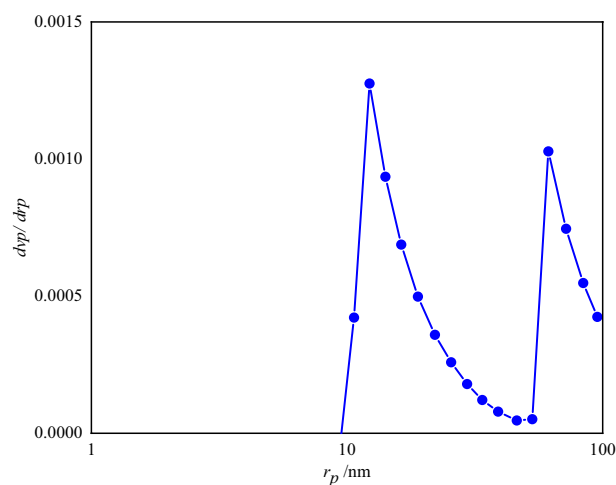


Figure 14. The BJH adsorption curve of the FSiPSS nano-catalyst.

Figure 14 shows the BJH adsorption curve of the FSiPSS nano-catalyst, which determined a pore size of approximately 12.24 nm.

Optimization of the reaction conditions. After synthesis and full characterization of the novel FSiPSS nano-catalyst, the catalytic performance of the prepared nanomagnetic catalyst was also evaluated in the synthesis of pyranopyrazole derivatives. To attain this target, the reaction of ethyl acetoacetate, hydrazine hydrate, malononitrile, and benzaldehyde in the presence of the FSiPSS nano-catalyst was selected as a model reaction to find the best reaction conditions. The resulting data in various temperatures, amounts of the catalyst, and solvents are outlined in Table 3. The obtained data indicate that the best results were achieved when the reaction is carried out in the presence of 20 mg of the FSiPSS nano-catalyst in ethanol at 40 °C under ultrasonic conditions

Entry	Solvent	Condition	Catal. amount (mg)	Time (min)	Yield (%)
1	C ₂ H ₅ OH	Sonication (50 Hz)/r.t	20	5	40
2	C₂H₅OH	Sonication (50 Hz)/40 °C	20	3	80
3	C ₂ H ₅ OH	Sonication (50 Hz)/50 °C	20	1	59
4	C ₂ H ₅ OH	Sonication (50 Hz)/60 °C	20	Fast	59
5	H ₂ O	Sonication (50 Hz)/40 °C	20	Fast	45
6	CH ₃ OH	Sonication (50 Hz)/40 °C	20	5	40
7	H ₂ O/C ₂ H ₅ OH	Sonication (50 Hz)/40 °C	20	2	31
8	Ethyl acetate	Sonication (50 Hz)/40 °C	20	3	35
9	<i>n</i> -Hexane	Sonication (50 Hz)/40 °C	20	–	–
10	CH ₃ Cl	Sonication (50 Hz)/40 °C	20	20	Trace
11	CH ₃ CN	Sonication (50 Hz)/40 °C	20	2	Trace
12	C ₂ H ₅ OH	Sonication (50 Hz)/40 °C	–	–	–
13	C ₂ H ₅ OH	Sonication (50 Hz)/40 °C	10	3	40
14	C ₂ H ₅ OH	Sonication (50 Hz)/40 °C	30	3	40
15	C ₂ H ₅ OH	Reflux	20	30	70

Table 3. Optimization of the reaction conditions for the synthesis of pyranopyrazoles. Significant values are in bold.

Entry	Catalyst	Condition	Time (min.)	Yield (%)	References
1	TEA-Im-IL-Cu	r.t	65	80	30
2	TrCl	Solvent-free, 60 °C	60	60	41
3	Cinchona alkaloid cupreine	CH ₂ Cl ₂ , r.t	27 h	92	46
4	FSi	Sonication/EtOH/40 °C	20	33	This work
5	FSiPS	Sonication/EtOH/40 °C	15	47	This work
6	FSiPSS	Sonication/EtOH/40 °C	3	80	This work

Table 4. Study of the effect of ultrasonication and the role of each part of the catalyst in the reaction.

(entry 2). In addition, the effect of ultrasonication was also studied and its significance can be observed in time of the reaction which is drastically reduced as demonstrated in Tables 3 and 4.

On other hand, the role of each part of the catalyst in the reaction was also investigated which the last step is the most effective according to entry 7 of Table 4.

Synthesis of diverse pyranopyrazoles 5(a-n). In the next step, with optimal reaction conditions in hand, the scope and generality of the presented method were investigated by examining the reaction of ethyl acetoacetate **1**, hydrazine hydrate **2**, various aromatic aldehydes **3(a-n)**, and malononitrile **4a** or ethyl cyanoacetate **4b** in the presence of the catalytic amount of the FSiPSS nano-catalyst under ultrasonic conditions (Table 5).

Proposed mechanism for the synthesis of diverse pyranopyrazoles 5(a-n). A plausible mechanism for this reaction is depicted in Fig. 15. According to our suggested mechanism, firstly, a nucleophilic attack of hydrazine **2** to the carbonyl group of the activated ethyl acetoacetate **1** gives intermediate **A**, which subsequently with loss of H₂O, and intramolecular nucleophilic attack of another NH₂ group of hydrazine to the next carbonyl group of ethyl acetoacetate generates 3-methyl-1*H*-pyrazol-5-ol (intermediate **B**). In the next step, the benzylidene (intermediate **C**) containing the electron-poor C=C double bond is afforded by Knoevenagel condensation of the active methylene **4a,b** to the aromatic aldehydes **3**. Finally, the Michael addition of intermediate **B** to C-2 of the resulting intermediate **C** affords intermediate **D**, that after the loss of proton and intramolecular cyclization afford pyrano[2,3-*c*]pyrazoles **5(a-n)** in moderate to good yields (40–80%).

Synthesis of ethyl 4-benzyl-5-imino-3-methyl-4,5-dihydro-1*H*-furo[2,3-*c*]pyrazole-4-carboxylate (5o) and the proposed mechanism. Interestingly, the reaction of ethyl acetoacetate **1**, hydrazine **2**, and benzaldehyde **3a** with ethyl cyanoacetate **4b** under the same condition results in the formation of ethyl 4-benzyl-5-imino-3-methyl-4,5-dihydro-1*H*-furo[2,3-*c*]pyrazole-4-carboxylate **5o** in 46% yield. In this reaction, the obtained intermediate **B** adds to the C-1 of the resulting intermediate **C**, which led to the formation of the intermediate **E** as indicated in Fig. 16. Subsequently, an intramolecular nucleophilic attack of the oxygen of the carbonyl group to the cyano group gives the desired pyrazole **5o**.

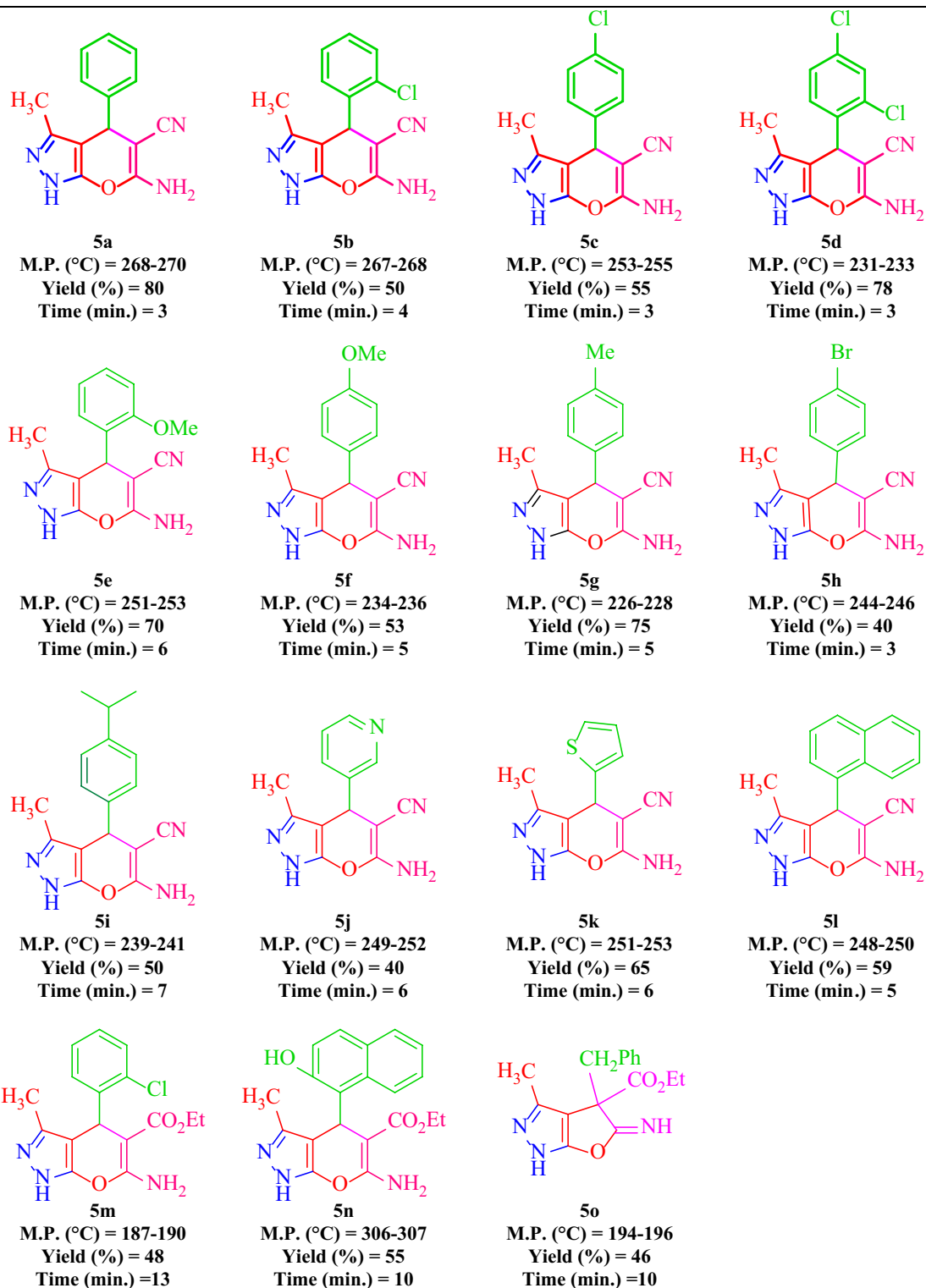


Table 5. Synthesis of pyranopyrazoles **5(a-n)** by application of the FSiPSS nano-catalyst. Reaction conditions: ethyl acetoacetate (1.0 mmol), hydrazine (1.0 mmol), aldehyde (1.0 mmol), malononitrile or ethyl cyanoacetate (1.5 mmol) and the FSiPSS nano-catalyst (20 mg) in EtOH (3.0 mL) under ultrasonic conditions.

Reusability of the FSiPSS nano-catalyst. In a separate study, recyclability and reusability of the magnetic FSiPSS nano-catalyst were tested for the synthesis of target molecule **5a** under optimal reaction conditions.

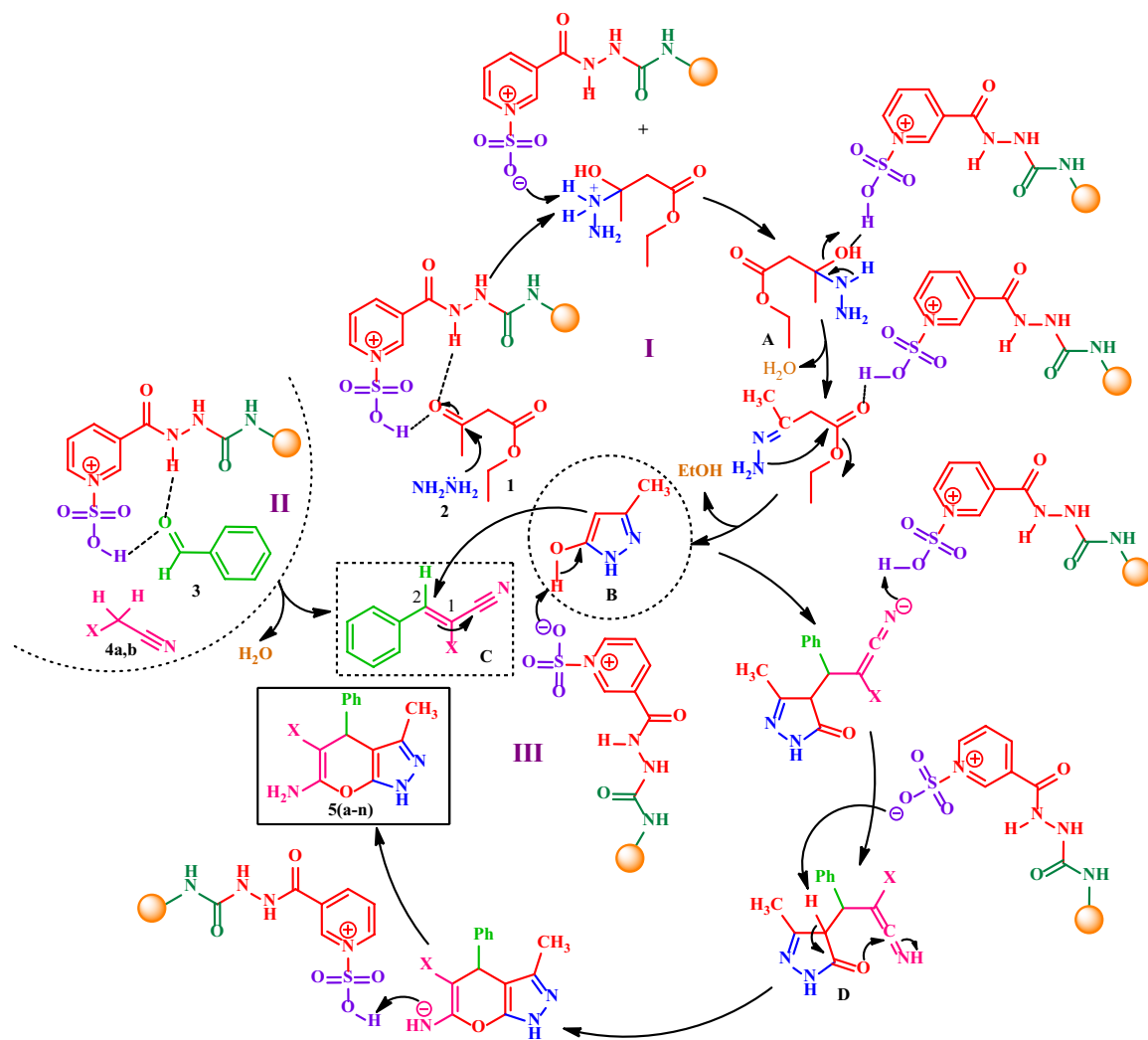


Figure 15. The proposed mechanism for the synthesis of diverse pyranopyrazoles 5(a-n).

At the end of each run, the magnetic FSiPSS nano-catalyst is separated from the reaction mixture by using a simple external magnet, washed thoroughly with EtOH, dried, and reused for the next run. Figure 17 demonstrates that the catalyst activity is preserved after four successive cycles without any considerable decrease in yield and reaction time.

Comparison of the catalyst activities. In addition, the efficiency of our proposed protocol was also evaluated comparatively with some previously reported methods for the synthesis of pyranopyrazoles. According to Table 6, our proposed protocol used in this paper for the synthesis of pyranopyrazoles has no disadvantages and is accessible, applicable, and reusable with a very short reaction time, good for high yields and easy work-up.

Conclusion

In summary, the synthesis of pyranopyrazole derivatives was performed using a sulfonic acid-functionalized nanomagnetic catalyst bearing the semicarbazide linkers as a new high-performance catalytic system under ultrasonic conditions. The simple and easy manufacturing procedure of this catalyst, along with the ability to recover and reuse it, makes it economical. The most attractive features of this procedure are low catalyst loading, short reaction times, good to high yields, lower temperature rather than previous works, compatibility with various functional groups, easy work-up, facile separation, and recyclability of catalyst.

Regarding the limitations of this project, the following points can be mentioned:

- Yield of the reaction: The yield of the reaction is between 40 and 80%, which can be improved in future by performing the reaction under new optimized conditions to increase the yield of the products.

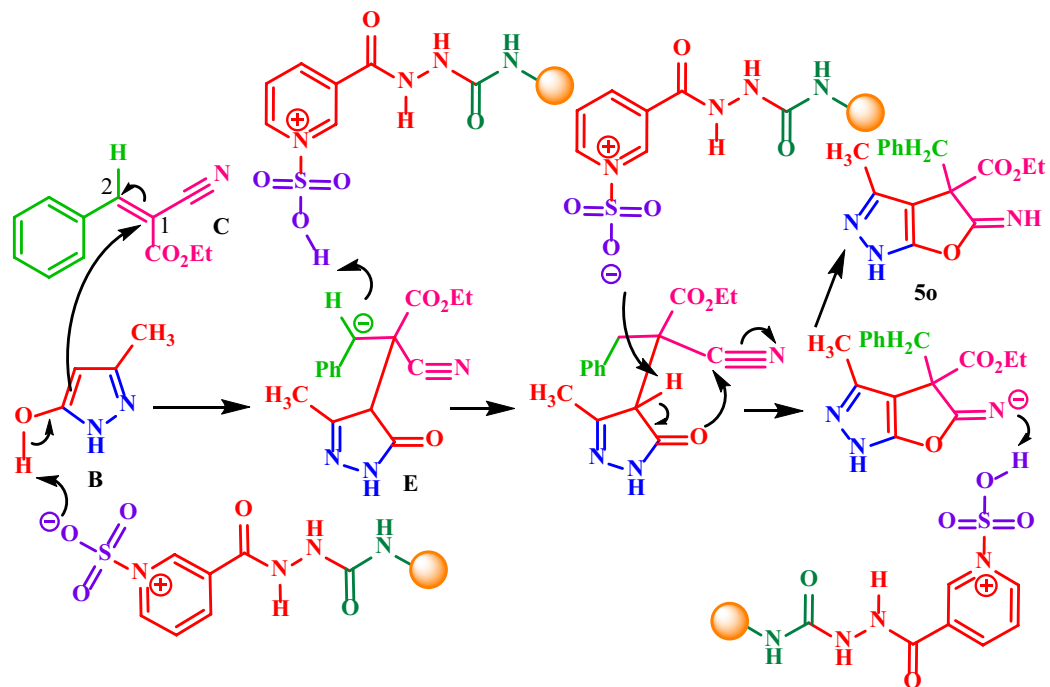


Figure 16. The proposed mechanism for the synthesis of the desired pyrazole **5o**.

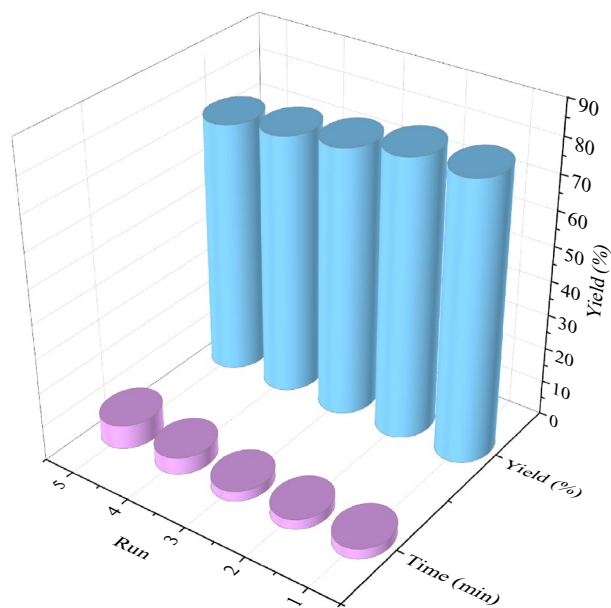


Figure 17. Reusability of the FSiPSS nano-catalyst.

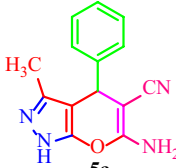
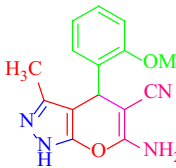
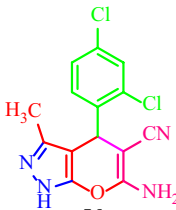
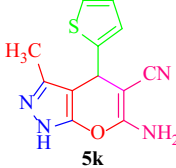
 <p>5a</p>	(1) TEA-Im-IL-Cu, rt, 65 min, 80% ³⁰
	(2) Isonicotinic acid (10 mol%), solvent-free, 85 °C, 10 min, 90% ³²
	(3) TrCl (10 mol%), solvent-free, 60 °C, 60 min, 80% ⁴¹
	(4) Cinchona alkaloid cupreine (5 mol%), CH ₂ Cl ₂ , rt, 27 h, 92% ⁴⁶
	(5) The FSiPSS nano-catalyst (20 mg), EtOH, 40 °C, ultrasonic, fast, 80% [Current work]
 <p>5e</p>	(1) TEA-Im-IL-Cu, rt, 25 min, 81% ³⁰
	(2) Isonicotinic acid (10 mol%), solvent-free, 85 °C, 25 min, 80% ³²
	(3) TrCl (10 mol%), solvent-free, 60 °C, 50 min, 83% ⁴¹
	(4) The FSiPSS nano-catalyst (20 mg), EtOH, 40 °C, ultrasonic, fast, 70% [Current work]
 <p>5d</p>	(1) Sodium ascorbate (15 mol%), EtOH:H ₂ O (2:1), 50 °C, 15 min, 82% ⁴⁸
	(2) Meglumine (10 mol%), EtOH:H ₂ O (9:1), rt, 17 min, 92% ⁴⁹
	(3) FSiPSS nano-catalyst (20 mg), EtOH, 40 °C, ultrasonic, fast, 78% [Current work]
 <p>5k</p>	(1) Isonicotinic acid (10 mol%), solvent-free, 85 °C, 15 min, 85% ³²
	(2) Sodium ascorbate (15 mol%), EtOH:H ₂ O (2:1), 50 °C, 12 min, 88% ⁴⁸
	(3) Meglumine (10 mol%), EtOH:H ₂ O (9:1), rt, 12 min, 92% ⁴⁹
	(4) FSiPSS nano-catalyst (20 mg), EtOH, 40 °C, ultrasonic, fast, 65% [Current work]

Table 6. Comparison of the prepared catalyst with other reported catalysts.

- Replacement of malononitrile with ethyl cyanoacetate: among derivatives synthesized with ethyl cyanoacetate, only 3 derivatives were purified. By changing the reaction conditions, we hope to reduce the number of side reactions and improving the purification of the products resulting from the reaction with ethyl cyanoacetate.

Data availability

All data generated or analyzed during this study are included in the supplementary information file.

Received: 9 April 2022; Accepted: 17 August 2022

Published online: 23 August 2022

References

1. Mulik, B. B., Munde, A. V., Dighole, R. P. & Sathe, B. R. Electrochemical determination of semicarbazide on cobalt oxide nanoparticles: Implication towards environmental monitoring. *J. Ind. Eng. Chem.* **93**, 259–266 (2021).
2. Wang, Y. & Chan, W. Automated in-injector derivatization combined with high-performance liquid chromatography–fluorescence detection for the determination of semicarbazide in fish and bread samples. *J. Agric. Food Chem.* **64**, 2802–2808 (2016).
3. Nan, C. *et al.* Stopped-flow kinetic analysis of the oxidation of semicarbazide by hexachloroiridate (IV). *Transit. Met. Chem.* **42**, 9–15 (2017).
4. Li, G. *et al.* A rapid and sensitive method for semicarbazide screening in foodstuffs by HPLC with fluorescence detection. *Food Anal. Methods* **8**, 1804–1811 (2015).

5. Asghar, S. F., Yasin, K. A., Habib-ur-Rehman, A. & Aziz, S. Synthesis and cyclisation of 1, 4-disubstituted semicarbazides. *Nat. Prod. Res.* **24**, 315–325 (2010).
6. Chen, M. N., Mo, L. P., Cui, Z. S. & Zhang, Z. H. Magnetic nanocatalysts: Synthesis and application in multicomponent reactions. *Curr. Opin. Green Sustain. Chem.* **15**, 27–37 (2019).
7. Osman, A. I., Abu-Dahrieh, J. K., McLaren, M., Laffir, F. & Rooney, D. W. Characterisation of robust combustion catalyst from aluminium foil waste. *ChemistrySelect* **3**, 1545–1550 (2018).
8. Xu, L., Zhang, S. Z., Li, W. & Zhang, Z. H. Visible-light-mediated oxidative amidation of aldehydes by using magnetic CdS quantum dots as a photocatalyst. *Eur. J. Chem.* **27**, 5483–5491 (2021).
9. Zhang, M., Liu, Y. H., Shang, Z. R., Hu, H. C. & Zhang, Z. H. Supported molybdenum on graphene oxide/Fe₃O₄: An efficient, magnetically separable catalyst for one-pot construction of spiro-oxindole dihydropyridines in deep eutectic solvent under microwave irradiation. *Catal. Commun.* **88**, 39–44 (2017).
10. Divband, B., Jodaie, A. & Khatamian, M. Enhancement of photocatalytic degradation of 4-nitrophenol by integrating Ag nanoparticles with ZnO/HZSM-5 nanocomposite. *Iran. J. Catal.* **9**, 63–70 (2019).
11. Farhadi, S., Ghasemzadeh, M. A. & Aghaei, S. S. NiCo₂O₄@ Ni (BDC) Nanoporous metal-organic framework as a novel catalyst for the synthesis of spiro [indene [1, 2-d] pyrimidine-ones and investigation of their antimicrobial activities. *ChemistrySelect* **4**, 729–736 (2019).
12. Mahapatra, A., Mishra, B. G. & Hota, G. Adsorptive removal of Congo red dye from wastewater by mixed iron oxide–alumina nanocomposites. *Ceram. Int.* **39**, 5443–5451 (2013).
13. Dadfar, S. M. *et al.* Iron oxide nanoparticles: Diagnostic, therapeutic and theranostic applications. *Adv. Drug Deliv. Rev.* **138**, 302–325 (2019).
14. Vallabani, N. V. & Singh, S. Recent advances and future prospects of iron oxide nanoparticles in biomedicine and diagnostics. *3 Biotech* **8**, 1–23 (2018).
15. Zhu, N. *et al.* Surface modification of magnetic iron oxide nanoparticles. *J. Nanomater.* **8**, 810 (2018).
16. Dinali, R., Ebrahiminezhad, A., Manley-Harris, M., Ghasemi, Y. & Berenjian, A. Iron oxide nanoparticles in modern microbiology and biotechnology. *Crit. Rev. Microbiol.* **43**, 493–507 (2017).
17. Dangolani, S. K., Panahi, F., Nourisefat, M. & Khalafi-Nezhad, A. 4-Dialkyl-aminopyridine modified magnetic nanoparticles: As an efficient nano-organocatalyst for one-pot synthesis of 2-amino-4H-chromene-3-carbonitrile derivatives in water. *RSC Adv.* **6**, 92316–92324 (2016).
18. Gao, G., Di, J. Q., Zhang, H. Y., Mo, L. P. & Zhang, Z. H. A magnetic metal-organic framework material as a highly efficient and recyclable catalyst for synthesis of cyclohexenone derivatives. *J. Catal.* **387**, 39–46 (2020).
19. Ghorbani-Vaghei, R. & Sarmast, N. Green synthesis of new pyrimido [4, 5-d] pyrimidine derivatives using 7-aminonaphthalene-1,3-disulfonic acid functionalized magnetic Fe₃O₄@ SiO₂ nanoparticles as catalyst. *Appl. Organomet. Chem.* **32**, e4003 (2018).
20. Mirhosseini-Eshkevari, B., Ghasemzadeh, M. A. & Safaei-Ghomi, J. An efficient and green one-pot synthesis of indazole [1,2-b]-phthalazinetriones via three-component reaction of aldehydes, dimedone, and phthalhydrazide using Fe₃O₄@SiO₂ core-shell nanoparticles. *Res. Chem. Intermed.* **41**, 7703–7714 (2015).
21. Safaei-Ghomi, J., Zahedi, S. & Ghasemzadeh, M. A. Nano silica-supported ferric chloride as a green and efficient catalyst for one-pot synthesis of 1, 2-dihydro-1-arylnaphtho [1,2-e][1,3] oxazine-3-ones. *Iran. J. Catal.* **2**, 27–30 (2012).
22. Maksoud, M. A. *et al.* Insight on water remediation application using magnetic nanomaterials and biosorbents. *Coord. Chem. Rev.* **403**, 213096 (2020).
23. Plohl, O. *et al.* Superior stability and high biosorbent efficiency of carboxymethylchitosan covalently linked to silica-coated core-shell magnetic nanoparticles for application in copper removal. *J. Environ. Chem. Eng.* **7**, 102913 (2019).
24. Mahmoudi, H., Jafari, A. A., Saeedi, S. & Firouzabadi, H. Sulfonic acid-functionalized magnetic nanoparticles as a recyclable and eco-friendly catalyst for atom economical Michael addition reactions and bis indolyl methane synthesis. *RSC Adv.* **5**, 3023–3030 (2015).
25. Avudaiappan, G., Unnimaya, T. J., Asha, P., Unnikrishnan, V. & Sreekumar, K. Green synthesis of pyrazolopyranopyrimidinone and pyranopyrazole derivatives using porphyrin-initiated amine-functionalized PolyBCMO dendritic polymer as sono-catalyst. *J. Heterocyclic Chem.* **57**, 197–209 (2020).
26. Dutta, A. *et al.* Catalyst-free UV365-assisted synthesis of pyran annulated heterocyclic scaffolds and evaluation of their antibacterial activities. *Synth. Commun.* **51**, 263–278 (2021).
27. Atar, A. B., Kim, J. T., Lim, K. T. & Jeong, Y. T. Synthesis of 6-amino-2,4-dihydro-pyrano[2,3-c]pyrazol-5-carbonitriles catalyzed by silica-supported tetramethyl-guanidine under solvent-free conditions. *Synth. Commun.* **44**, 2679–2691 (2014).
28. Kiyani, H. & Ghorbani, F. Efficient tandem synthesis of a variety of pyran-annulated heterocycles, 3,4-disubstituted isoxazol-5(4H)-ones, and α , β -FSiPS saturated nitriles catalyzed by potassium hydrogen phthalate in water. *Res. Chem. Intermed.* **41**, 7847–7882 (2015).
29. Maleki, A. & Eskandarpour, V. Design and development of a new functionalized cellulose-based magnetic nanocomposite: Preparation, characterization, and catalytic application in the synthesis of diverse pyrano[2,3-c]pyrazole derivatives. *J. Iran Chem. Soc.* **16**, 1459–1472 (2019).
30. Ghafari, H., Kazemnezhad Leili, M. & Esmaili Zand, H. R. Copper-immobilized ionic liquid as an alternative to organic solvents in the one-pot synthesis of bioactive dihydropyrano[2,3-c]pyrazole derivatives. *Appl. Organomet. Chem.* **34**, e5757 (2020).
31. Beerappa, M. & Shivashankar, K. Four component synthesis of highly functionalized pyrano[2,3-c]pyrazoles from benzyl halides. *Synth. Commun.* **48**, 146–154 (2018).
32. Zolfigol, M. A. *et al.* Synthesis of pyranopyrazoles using isonicotinic acid as a dual and biological organocatalyst. *RSC Adv.* **3**, 25681–25685 (2013).
33. Wu, M., Feng, Q., Wan, D. & Ma, J. CTACl as catalyst for four-component, one-pot synthesis of pyranopyrazole derivatives in aqueous medium. *Synth. Commun.* **43**, 1721–1726 (2013).
34. Xiao, Z., Lei, M. & Hu, L. An unexpected multi-component reaction to synthesis of 3-(5-amino-3-methyl-1H-pyrazol-4-yl)-3-arylpropanoic acids in ionic liquid. *Tetrahedron Lett.* **52**, 7099–7102 (2011).
35. Swaroop, T. R., Sharath-Kumar, K. S., Palanivelu, M., Chaitanya, S. & Rangappa, K. S. A catalyst-free green protocol for the synthesis of pyranopyrazoles using room temperature ionic liquid choline chloride-urea. *J. Heterocyclic Chem.* **51**, 1866–1870 (2014).
36. Shinde, S. K., Patil, M. U., Damate, S. A. & Patil, S. S. Synergetic effects of naturally sourced metal oxides in organic synthesis: A greener approach for the synthesis of pyrano[2,3-c]pyrazoles and pyrazolyl-4H-chromenes. *Res. Chem. Intermed.* **44**, 1775–1795 (2018).
37. Shaterian, H. R. & Kangani, M. Synthesis of 6-amino-4-aryl-3-methyl-1, 4-dihydro-pyrano[2,3-c]pyrazole-5-carbonitriles by heterogeneous reusable catalysts. *Res. Chem. Intermed.* **40**, 1997–2005 (2014).
38. Rather, R. A. & Siddiqui, Z. N. Synthesis, characterization and application of Nd-salen Schiff base complex immobilized mesoporous silica in solvent free synthesis of pyranopyrazoles. *J. Organomet. Chem.* **868**, 164–174 (2018).
39. Paul, S., Pradhan, K., Ghosh, S., De, S. K. & Das, A. R. Uncapped SnO₂ quantum dot catalyzed cascade assembling of four components: A rapid and green approach to the pyrano[2,3-c]pyrazole and spiro-2-oxindole derivatives. *Tetrahedron* **70**, 6088–6099 (2014).
40. Thongni, A., Phanrang, P. T., Dutta, A. & Nongkhaw, R. One-pot synthesis of 2-amino-3-cyano-4H-pyrans and pyran-annulated heterocycles using sodium citrate as an organo-salt based catalyst in aqueous ethanol. *Synth. Commun.* **2**, 1–20 (2021).

41. Moosavi-Zare, A. R., Zolfigol, M. A. & Mousavi-Tashar, A. Synthesis of pyrano-pyrazole derivatives by in situ generation of trityl carbocation under mild and neutral media. *Res. Chem. Intermed.* **42**, 7305–7312 (2016).
42. Maddila, S. N., Maddila, S., van Zyl, W. E. & Jonnalagadda, S. B. CeO₂/ZrO₂ as green catalyst for one-pot synthesis of new pyrano[2,3-*c*]pyrazoles. *Res. Chem. Intermed.* **43**, 4313–4325 (2017).
43. Kangani, M. *et al.* Green procedure for the synthesis of 1,4-dihydro pyrano[2,3-*c*]pyrazoles using saccharose. *J. Iran Chem. Soc.* **12**, 47–50 (2015).
44. Kanagaraj, K. & Pitchumani, K. Solvent-free multicomponent synthesis of pyrano-pyrazoles: Per-6-amino- β -cyclodextrin as a remarkable catalyst and host. *Tetrahedron Lett.* **51**, 3312–3316 (2010).
45. Shaikh, M. A., Farooqui, M. & Abed, S. Novel task-specific ionic liquid [Et₃NH (CH₂)₂CO₂H][AcO] as a robust catalyst for the efficient synthesis of some pyran-annulated scaffolds under solvent-free conditions. *Res. Chem. Intermed.* **45**, 1595–1617 (2019).
46. Gogoi, S. & Zhao, C. G. Organocatalyzed enantioselective synthesis of 6-amino-5-cyanodihydropyrano[2,3-*c*]pyrazoles. *Tetrahedron Lett.* **50**, 2252–2255 (2009).
47. Liang, Y., Dong, Y., Sun, G., Su, Z. & Guan, W. Theoretical mechanistic study of 4CzIPN/Ni⁰-metallaphotoredox catalyzed enantioselective desymmetrization of cyclic meso-anhydrides. *Dalton Trans.* **50**, 17675–17687 (2021).
48. Kiyani, H. & Bamdad, M. Sodium ascorbate as an expedient catalyst for green synthesis of polysubstituted 5-aminopyrazole-4-carbonitriles and 6-amino-1,4-di-hydropyrano[2,3-*c*]pyrazole-5-carbonitriles. *Res. Chem. Intermed.* **44**, 2761–2778 (2018).
49. Guo, R. Y. *et al.* Meglumine promoted one-pot, four-component synthesis of pyranopyrazole derivatives. *Tetrahedron* **69**, 9931–9938 (2013).
50. Habibi, D., Pakravan, N., Arabi, A. & Kaboudvand, Z. Preparation of Fe₃O₄@5,10-dihydropyrido[2,3-*b*]quinoxaline-7,8-diol copper complex: A capable nanocatalyst for the green synthesis of 1-substituted 1*H*-tetrazoles. *Appl. Organomet. Chem.* **32**, e3988 (2018).
51. Ariannezhad, M., Habibi, D. & Heydari, S. Copper nanoparticles: A capable and versatile catalyst for the synthesis of diverse 1-phenyl-1*H*-tetrazoles from amino acids. *Polyhedron* **160**, 170–179 (2019).
52. Ariannezhad, M., Habibi, D., Heydari, S. & Khorramabadi, V. A new supported Mn-based coordination complex as a nano-catalyst for the synthesis of indazolophthalazinetriones and investigation of its antibacterial activity. *Chemistry* **3**, 783–799 (2021).
53. Khorramabadi, V., Habibi, D. & Heydari, S. Facile synthesis of tetrazoles catalyzed by the new copper nano-catalyst. *Green Chem. Lett. Rev.* **13**, 50–59 (2020).
54. Mansouri, M., Habibi, D. & Heydari, S. The phenyltetrazolethiol-based nickel complex: A versatile catalyst for the synthesis of diverse amidoalkyl naphthols and chromenes. *Res. Chem. Intermed.* **23**, 1–20 (2021).
55. Aghayee, M., Zolfigol, M. A., Keypour, H., Yarie, M. & Mohammadi, L. Synthesis and characterization of a novel magnetic nanopalladium Schiff base complex: Application in cross-coupling reactions. *Appl. Organomet. Chem.* **30**, 612–618 (2016).
56. Jian, X. *et al.* Hetero-structured nanorings of Fe–Fe₃O₄@C hybrid with enhanced microwave absorption performance. *ACS Appl. Mater. Interfaces* **10**, 9369–9378 (2018).
57. Zhang, M. *et al.* Magnetically separable graphene oxide anchored sulfonic acid: A novel, highly efficient and recyclable catalyst for one-pot synthesis of 3,6-di(pyridin-3-yl)-1*H*-pyrazolo[3,4-*b*]pyridine-5-carbonitriles in deep eutectic solvent under microwave irradiation. *RSC Adv.* **6**, 106160–106170 (2016).
58. Sun, L. *et al.* Porphyrin-functionalized Fe₃O₄@SiO₂ core-shell magnetic colorimetric material for detection, adsorption and removal of Hg²⁺ in aqueous solution. *New J. Chem.* **35**, 2697–2704 (2011).
59. Mohammadi, M. & Ghorbani-Choghamarani, A. Synthesis and characterization of novel mercynite@sulfuric acid and its catalytic applications in the synthesis of polyhydro-quinolines and 2,3-dihydroquinazolin-4 (1*H*)-ones. *RSC Adv.* **12**, 2770–2787 (2022).
60. Thommes, M. *et al.* Physisorption of gases, with special reference to the evaluation of surface area and pore size distribution (IUPAC Technical Report). *Pure Appl. Chem.* **87**, 1051–1069 (2015).

Acknowledgements

The authors are grateful to the Bu-Ali Sina University for the support of this work.

Author contributions

My PhD student Miss M.B. wrote the main manuscript text and the manuscript was checked, reviewed, amended and rewritten by me (Prof D.H.).

Competing interests

The authors declare no competing interests.

Additional information

Supplementary Information The online version contains supplementary material available at <https://doi.org/10.1038/s41598-022-18651-5>.

Correspondence and requests for materials should be addressed to D.H.

Reprints and permissions information is available at www.nature.com/reprints.

Publisher's note Springer Nature remains neutral with regard to jurisdictional claims in published maps and institutional affiliations.



Open Access This article is licensed under a Creative Commons Attribution 4.0 International License, which permits use, sharing, adaptation, distribution and reproduction in any medium or format, as long as you give appropriate credit to the original author(s) and the source, provide a link to the Creative Commons licence, and indicate if changes were made. The images or other third party material in this article are included in the article's Creative Commons licence, unless indicated otherwise in a credit line to the material. If material is not included in the article's Creative Commons licence and your intended use is not permitted by statutory regulation or exceeds the permitted use, you will need to obtain permission directly from the copyright holder. To view a copy of this licence, visit <http://creativecommons.org/licenses/by/4.0/>.

© The Author(s) 2022